A terrestrial magmatic hibonite-grossite-vanadium assemblage: Desilication and extreme reduction in a volcanic plumbing system, Mount Carmel, Israel

WILLIAM L. GRIFFIN[1,*,†], SARAH E.M. GAIN[1], JIN-XIANG HUANG[1], MARTIN SAUNDERS[2], JEREMY SHAW[2], VERED TOLEDO[3], AND SUZANNE Y. O'REILLY[1]

[1]ARC Centre of Excellence for Core to Crust Fluid Systems (CCFS) and GEMOC, Earth and Planetary Sciences, Macquarie University, New South Wales 2109, Australia ORCID 0000-0002-0980-2566
[2]Centre for Microscopy, Characterisation and Analysis, The University of Western Australia, Western Australia 6009, Australia
[3]Shefa Yamim (A.T.M.) Ltd., Netanya 4210602, Israel

ABSTRACT

Hibonite ($CaAl_{12}O_{19}$) is a constituent of some refractory calcium-aluminum inclusions (CAIs) in carbonaceous meteorites, commonly accompanied by grossite ($CaAl_4O_7$) and spinel. These phases are usually interpreted as having condensed, or crystallized from silicate melts, early in the evolution of the solar nebula. Both Ca-Al oxides are commonly found on Earth, but as products of high-temperature metamorphism of pelitic carbonate rocks. We report here a unique occurrence of magmatic hibonite-grossite-spinel assemblages, crystallized from Ca-Al-rich silicate melts under conditions [high-temperature, very low oxygen fugacity (f_{O_2})] comparable to those of their meteoritic counterparts. Ejecta from Cretaceous pyroclastic deposits on Mt Carmel, N. Israel, include aggregates of hopper/skeletal Ti-rich corundum, which have trapped melts that crystallized at f_{O_2} extending from 7 log units below the iron-wustite buffer ($\Delta IW = -7$; SiC, Ti_2O_3, Fe-Ti silicide melts) to $\Delta IW \leq -9$ (native V, TiC, and TiN). The assemblage hibonite + grossite + spinel + TiN first crystallized late in the evolution of the melt pockets; this hibonite contains percentage levels of Zr, Ti, and REE that reflect the concentration of incompatible elements in the residual melts as corundum continued to crystallize. A still later stage appears to be represented by coarse-grained (centimeter-size crystals) ejecta that show the crystallization sequence: corundum + Liq $\rightarrow$ (low-REE) hibonite $\rightarrow$ grossite + spinel $\pm$ krotite $\rightarrow$ $Ca_4Al_6F_2O_{12}$ + fluorite. V^0 appears as spheroidal droplets, with balls up to millimeter size and spectacular dendritic intergrowths, included in hibonite, grossite, and spinel. Texturally late V^0 averages 12 wt% Al and 2 wt% Mn. Spinels contain 10–16 wt% V in V^0-free samples, and <0.5 wt% V in samples with abundant V^0. Ongoing paragenetic studies suggest that the f_{O_2} evolution of the Mt Carmel magmatic system reflects the interaction between OIB-type mafic magmas and mantle-derived CH_4+H_2 fluids near the crust-mantle boundary. Temperatures estimated by comparison with 1 atm phase-equilibrium studies range from ca. 1500 °C down to 1200–1150 °C. When f_{O_2} reached ca. $\Delta IW = -7$, the immiscible segregation of Fe,Ti-silicide melts and the crystallization of SiC and TiC effectively desilicated the magma, leading to supersaturation in Al_2O_3 and the rapid crystallization of corundum, preceding the development of the hibonite-bearing assemblages. Reports of Ti-rich corundum and SiC from other areas of explosive volcanism suggest that these phenomena may be more widespread than presently realized, and the hibonite-grossite assemblage may serve as another indicator to track such activity.

This is the first reported terrestrial occurrence of krotite ($CaAl_2O_4$), and of at least two unknown Zr-Ti oxides.

Keywords: Hibonite, native vanadium, grossite, krotite, super-reduced conditions, mantle methane, Mt Carmel; Volatile Elements in Differentiated Planetary Interiors

INTRODUCTION

Hibonite ($CaAl_{12}O_{19}$) was described as a new mineral in 1956 (Curien et al. 1956) and is named after Paul Hibon, who found centimeter-sized black crystals in a placer deposit in Madagascar in 1953. It is a constituent of some refractory calcium-aluminum inclusions (CAIs) in carbonaceous chondrites, commonly asso-

ciated with grossite ($CaAl_4O_7$) and corundum (Grossman et al. 1988; Beckett et al. 2006). Hibonite also occurs as microscopic grains in meteorites, and it is one of the oldest minerals in the solar system.

The type locality of hibonite is the Esiva alluvial deposits, in Tulear Province, Madagascar. The material was probably derived from nearby deposits of thorianite-bearing skarns, which are widespread in the Pan-African (565–515 Ma) granulite belts of Madagascar and Tanzania (Rakotondrazafy et al. 1996). In these rocks, early corundum + spinel + scapolite assemblages

are altered to anorthite + calcite + less-calcic scapolite, while hibonite crystallized at the expense of corundum and spinel. Hibonite also occurs as tabular crystals up to 3 cm across in calcitic marbles from the Tashelga-Malzaskaya region in Siberia (Konovalenko et al. 2012). These metamorphic hibonites are notably high in Fe^{3+}, and they coexist with V-rich minerals (goldmanite, tashelgite, mukhinite). *P-T* conditions are estimated at 700–800 °C and 3.5 kbar. The crystallization of hibonite implies a very low silica activity and, in this location, probably high CO_2.

The type locality of grossite is the Hatrurim formation (formerly known as the "Mottled Zone"), a unique rock complex exposed mainly in the Judean Desert of Israel, where it was first described by Gross (1977). The formation was deposited as a thin marine, bituminous chalk-marl formation of Campanian to Neogene age. However, at several localities, it is metamorphosed to the sanidinite and pyroxene-hornfels facies (up to 1000 °C, very low *P*), due to spontaneous isochemical combustion of bituminous compounds. Hibonite and grossite are widespread in these metamorphosed sediments.

All previously known terrestrial occurrences of hibonite and grossite are, to our knowledge, metamorphic in origin. In contrast, the textures of hibonite-bearing CAIs in CV chondrites are ambiguous; hibonite occurs as a minor phase coexisting with melilite, or in coarse-grained assemblages that could be metamorphic. However, CAIs from CM chondrites are dominated by assemblages such as hibonite + spinel + perovskite, some of which contain glass. Textural features are consistent with crystallization of hibonite from Al-rich melts (Kurat et al. 1975; Grossman et al. 1988; Ireland et al. 1991), condensed from the solar nebula. The predicted sequence of crystallization would be corundum-hibonite-perovskite, with subsequent reactions leading to melilite and spinel. The condensation and crystallization of such melts would require temperatures of ca. 1500–1300 °C and would have occurred at the very low oxygen fugacity (f_{O_2}) imposed by the hydrogen-dominated composition of the early solar nebula (Yoneda and Grossman 1995; Grossman et al. 2008).

The apparent absence of magmatic hibonite-grossite assemblages on Earth thus is understandable. However, we report here a terrestrial analog to the hibonite-bearing CAIs of CM chondrites, from the Mt Carmel volcanics of northern Israel. Our aim is to document these unusual parageneses; define their relationships to other members of the ultra-reduced Mt Carmel volcanic system (Griffin et al. 2016, 2018; Xiong et al. 2017); discuss briefly the mechanisms that can produce similar high-*T*, low-f_{O_2} environments on Earth, and indicate its implications for the behavior of carbon in deep-seated volcanic systems.

BACKGROUND

Several years of exploration for placer gemstone deposits in the drainage of the Kishon River, which enters the sea near Haifa in northern Israel (Supplemental[1] Fig. S1), have provided this unusual occurrence of hibonite and grossite. Details of the geologic setting of pyroclastic host rocks are given in (Griffin et al. 2016).

Aggregates of hopper-formed corundum crystals ("Carmel Sapphire") are common in the pyroclastic ejecta of the volcanoes exposed on Mt Carmel, and in associated alluvial deposits. Melt pockets trapped within and between the skeletal corundum crystals contain mineral assemblages including moissanite (SiC),

Fe-Ti-Zr silicides/phosphides, Ti nitrides and borides, and native V that require high *T* (≥1450 to ca. 1200 °C) and f_{O_2} from 6 to 9 log units more reducing than the iron-wustite buffer ($\Delta IW = -6$ to -9).

Paragenetic studies (Griffin et al. 2016, 2018; Xiong et al. 2017; Fig. 1) suggest that the crystallization of corundum and the low f_{O_2} reflect the interaction of basaltic magmas with mantle-derived $CH_4 + H_2$ at high fluid/melt ratios, leading to progressive reduction and desilication of the magma, and ultimately to Al_2O_3-supersaturation, the rapid growth of skeletal/hopper corundum crystals, and the deposition of abundant amorphous carbon. This evolution included several stages of liquid-liquid immiscibility, including the segregation of Fe- and Ti-silicide melts from silicate melts, driven by a progressive decrease in f_{O_2}. The latest stage of this evolution is defined by the appearance of hibonite, grossite, and spinel, suggesting that silica-deficient melts evolved beneath some of the volcanic centers.

METHODS

The samples, collected and provided by Shefa Yamim, have been mounted in epoxy disks, polished, and characterized by optical microscopy, backscattered electron microscopy, and cathodoluminescence imaging in the scanning electron microscope to identify minerals and to establish parageneses. Mineral compositions were analyzed by both SEM-EDS and WDS electron microprobe. Trace elements were analyzed by LA-ICP-MS. Selected samples were examined by TEM using FIB foils, and TEM-EDS and TEM-XRD were used to obtain chemical analyses and crystallographic parameters of specific phases. 3D-μCT scans of individual grains and aggregates were taken to examine structures in three dimensions. Details of each of these methods are given in the Supplementary[1] Data.

Petrography

HIbonite from the primary pyroclastic deposits and in placer samples from the Kishon and Yoqneam Rivers occurs in two parageneses. Paragenesis A comprises inclusions in and between skeletal corundum crystals, and paragenesis B the granular aggregates of hibonite + grossite + spinel.

Paragenesis A: Hibonite in corundum

Hibonite occurs in pockets of trapped melt interstitial to, or included in, corundum crystals within the corundum aggregates (Figs. 2 and 3). The melt pockets in the corundum aggregates have been described by Griffin et al. (2016, 2018) and Xiong et al. (2017). The earliest parageneses consist of tistarite (Ti_2O_3) ± carmeltazite ($ZrTi_2Al_4O_{11}$; Griffin et al. 2019) ± Mg-Al spinel in a matrix of Ca-Mg-Al-Si-O glass. The earliest trapped melts represent a considerable modification of assumed primary silicate melts (probably basaltic), including progressive desilication by the exsolution of immiscible Fe-Ti oxide melts and Fe-Ti-Zr-silicide melts, and the crystallization of moissanite and khamrabaevite (TiC), at $f_{O_2} = \Delta IW$-6 or less. This process continued, producing progressively lower f_{O_2}, witnessed especially by the appearance of Ti^{2+}-bearing phases (TiB_2, TiN, TiC, TiO). The earliest appearance of hibonite in the melt pockets is in association with carmeltazite, spinel, TiN, Fe-Ti silicides and TiC in glass, interstitial to corundum crystals (Fig. 2). This hibonite is locally associated with grossite but appears also to be in textural equilibrium with corundum. In some pockets, hibonite is intergrown with or crosscut by at least two unknown Zr-Ti oxides. (Supplemental[1] Table S1; Fig. 3). These phases and others (Supplemental[1] Table S1) appear to reflect the continuous concentration of incompatible elements in the silicate melts (percent levels of Ti, Zr, La, and Ce; Table 1) as the trapped melt volumes were progressively reduced by the growth of corundum, in parallel with the decrease in f_{O_2}.

Paragenesis B: Hibonite-grossite aggregates

Rounded to angular grains ranging from millimeters up to 2.5 cm across consist of flattened hexagonal prisms (*a:c* = 7–17) of hibonite in a matrix of grossite and Mg-Al spinel (Fig. 4). The rough material typically is purplish in color (Fig. 4a), but in polished, more transparent grains some have a yellow-orange color. The hibonite displays orange cathodoluminescence, while that of grossite is blue to purple. A characteristic feature is the occurrence of balls and dendrites of native vanadium, included in hibonite and grossite, and more rarely in spinel.
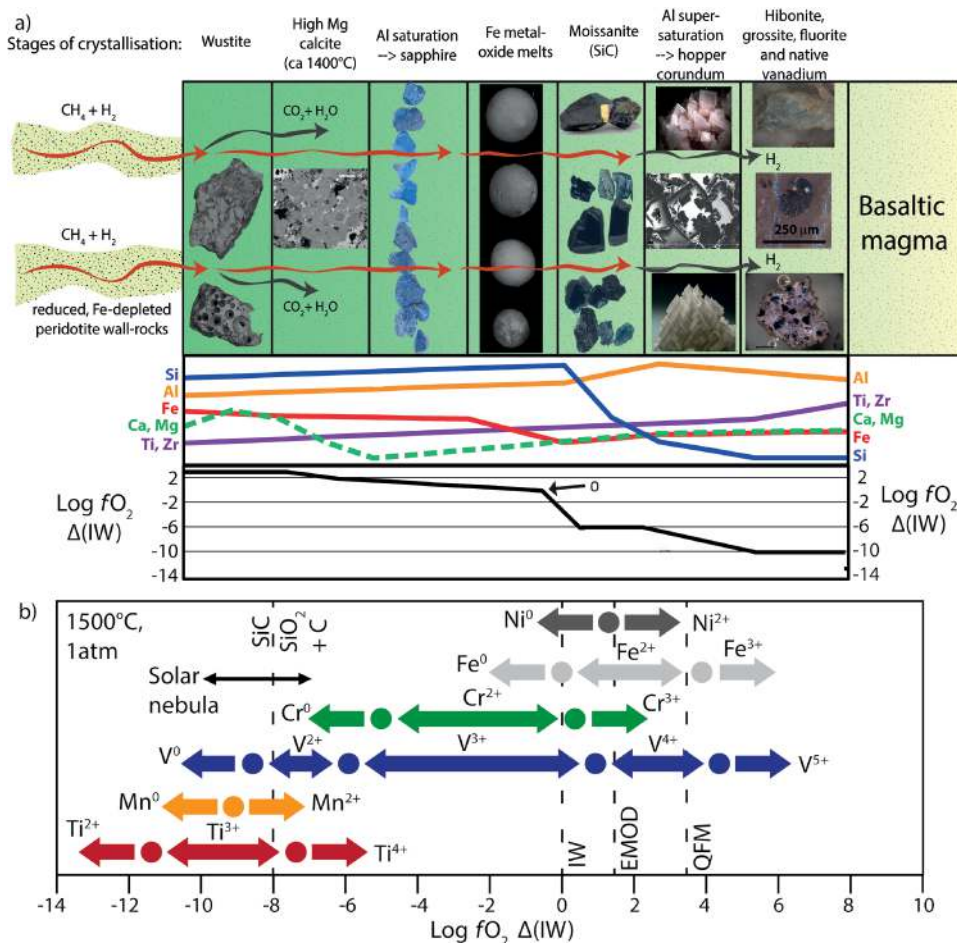
FIGURE 1. (**a**) Schematic evolution of a mafic magmatic system progressively reduced by interaction with mantle-derived CH_4+H_2 fluids. Boxes illustrate the reconstructed sequence of mineral assemblages; the relative variations in major elements through this process are not to scale, but are intended to emphasize the effects of reduction, crystallization, and the immiscibility of silicide melts. (**b**) Relative positions of relevant f_{O_2} buffers at 1500 °C, 1 atm (after Papike et al. 2013). (Color online.)

The major paragenesis of these intergrowths is shown in Figures 5 to 7. Hibonite occurs as tabular crystals up to 1 cm across, in a matrix of granular grossite and spinel (commonly as euhedral octahedra); fluorite is the last phase to crystallize. Resorbed remnants of corundum in some hibonite laths (Figs. 5 and 6) indicate that corundum crystallized before the Ca-Al-oxides and that hibonite crystallized via the peritectic reaction corundum (Cor) + liquid/melt (L) → hibonite. This was followed by the cotectic precipitation of grossite, hibonite, and spinel, and finally the assemblage grossite + spinel + $CaAl_2O_4$ (krotite) + fluorite.

Grossite commonly is euhedral against interstitial fluorite. The oxyfluoride phase $Ca_4Al_6F_2O_{12}$ (widely synthesized, but not previously reported in nature) appears to precede fluorite in the crystallization sequence and to coexist with grossite. Rare grains of perovskite ($CaTiO_3$) also appear to coexist with grossite (Fig. 5c; Supplemental[1] Table S1) or intergrown with fluorite (Fig. 5d).

Most of the hibonite-grossite aggregates show little or no preferred orientation of the hibonite crystals, but some have radiating structures. In the example shown in Supplemental[1] Figure S2, the hibonite + grossite + spinel + fluorite assemblage appears to have grown from a substrate of coarse-grained grossite; the width of the hibonite tablets increases with distance from the contact, suggesting a quench-related structure.

Small drop-like grains of native vanadium (V^0) are common in hibonite and grossite (Fig. 5a and 5b), indicating the lowering of f_{O_2} to ΔIW ≤ –9, where V^0 becomes stable (Fig. 1). It occurred roughly at the temperature of the peritectic reaction cor + L = hibonite, although there is no obvious reason for the two reactions to be linked. Native V also occurs as balls up to 500 μm across, either isolated within hibonite or together with grossite and fluorite in complex pockets among hibonite grains (Fig. 8a). These larger balls contain percent levels of Cr and Mn and have exsolved into laths of V^0

with higher and lower levels of these two elements (Figs. 8b and 8c; Supplemental[1] Table S1). Some of these balls are altered to mixtures of fluorite and carbonates (Fig. 8d) related to cracks, some of which are filled with an Al-hydroxide, possibly gibbsite. Larger cracks contain pockets with a geode-like zoned filling of this phase, including terminated crystals extending into open voids. Since the assemblage V^0 + CaF_2 apparently is stable in other situations (Fig. 8a), this alteration is interpreted as a post-eruption phenomenon.

In some cases, vanadium in hibonite develops from drop-like balls with worm-like protuberances (Fig. 8), into spectacular 3D dendritic growths (Fig. 9; Supplemental[1] Fig. S3), growing sub-parallel to the c axis of the hibonite crystals.

MINERAL CHEMISTRY

Major and minor elements

Hibonite included in corundum (paragenesis A) contains significant levels of Si, Zr, Ti, Cr, Sr, Mg, and LREE (up to >6% Ce_2O_3; Supplemental[1] Table S1), but does not contain measurable levels of V. TEM imaging shows a hexagonal cell with c = 22.73 Å, compared to 22.29 Å in the type material; the a axis is 4.8 Å, shorter than in the type material (5.6 Å). Calculation of the structural formula on the basis of 19 O atoms indicates that essentially all of the Ti is present as Ti^{3+}. The apparent deficit in trivalent ions in the formula (Supplemental[1] Table S1) probably
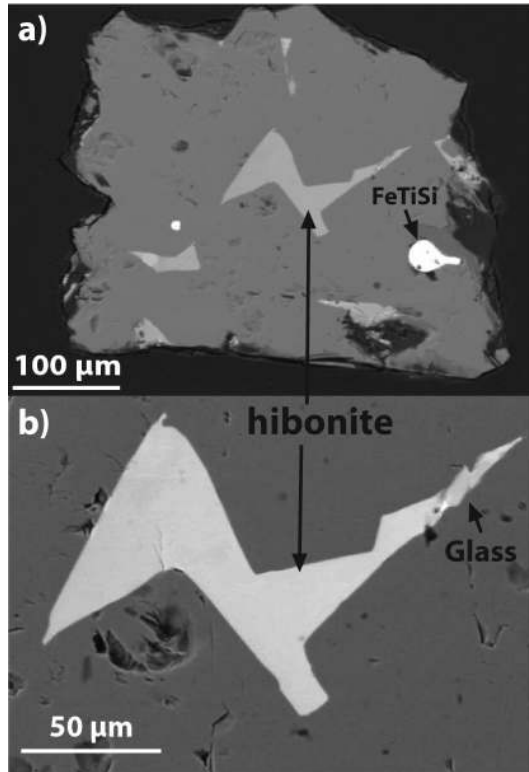
FIGURE 2. Hibonite in corundum. (**a**) BSE image of hibonite and associated phases in melt pocket in corundum. (**b**) Close-up BSE image of hibonite; note euhedral terminations on corundum crystals, and residual glass in the outermost thin wedge.
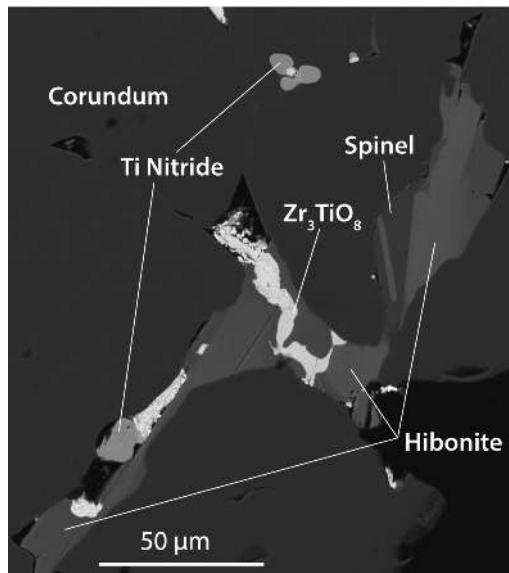

FIGURE 3. Zr_3TiO_8 "phase" with irregular borders crosscutting hibonite in melt pocket in corundum; note presence of spinel. The Zr_3TiO_8 phase is heterogeneous on a small scale, as reflected in its speckled appearance, and breaks up in contact with Ca-Mg-Al-oxide glass (black), suggesting that both were melts during emplacement of the Zr_3TiO_8 phase.

reflects the levels of other REE (see below) that are below the detection limit of the EMP (ca. 0.1 wt%). In contrast, hibonite in the granular aggregates (paragenesis B) contains percent levels of V, and minor levels of Mg, but all other elements are below detection for the EMP. Calculation of the structural formula (Supplemental[1] Table S1) suggests that V is present as V^{3+}, or even partly as V^{2+}.

Grossite is essentially stoichiometric $CaAl_4O_7$ with no minor elements at the EMP level. The Raman spectrum of the stoichiometric phase $CaAl_2O_4$ (Supplemental[1] Table S1) identifies it as the low-pressure form krotite, rather than the high-pressure form dimitryivanovite. This is consistent with available pressure constraints (see below) that suggest crystallization at around 1 GPa, while dimitryivanovite is stable above 2 GPa (Mikouchi et al. 2009). To our knowledge, this is the first natural terrestrial occurrence of krotite, originally described from a CAI in a CV3 carbonaceous chondrite (Ma et al. 2011).

Spinels occurring in melt pockets with hibonite (paragenesis A) are essentially pure Mg-Al spinels, with a deficit in Mg and an

TABLE 1. Trace-element compositions of selected phases

	Hibonite A		Hibonite B		Grossite B		Spinel B	
	mean n = 2	St.dev.	mean n = 9	St.dev.	mean n = 7	St.dev.	mean n = 4	St.dev.
Li	59.1		<1.5				7.46	0.98
Be	10.0		<0.2				<0.3	
B	19.2		30.0	16.7	27.9	19.0	29.9	5.83
Na	45		24.0	13.3	90.7	12.0	332	267
Mg	11863		3700	875	542	49	149364	14403
Si	4777		1302	540	1017	676	1135	185
P	3.4		55.1	23.6	31.6	22.4	55.8	14.4
K	104		<5		<5		48.2	63.2
Sc	171		<0.5		0.22	0.37	<0.7	
Ti	16777		291	206	58.4	32.1	153	24.3
V	1.8		6002	3358	1804	748	25517	2437
Cr	0.2		13.9	9.30	6.55	5.0	76.5	20.2
Mn	34		207	192	249	139	4361	1402
Fe	<20		67.4	23.1	166	49	<30	
Co	<0.1		<0.1		0.05	0.06	<0.2	
Ni	3.5		<0.5		0.24	0.26	<0.5	
Cu	<0.2		<0.2		0.01	0.02	<0.3	
Zn	0.02		<1		0.60	0.75	9.60	2.0
Ga	7.6		0.42	0.4	0.03	0.05	<0.2	
Rb	<0.5		<0.2		<0.15		<0.2	
Sr	9889		76.4	26.9	34.7	10.1	<7	
Y	407		3.10	0.6	3.89	0.77	0.06	0.01
Zr	3468		5.21	3.7	0.12	0.24	<0.1	
Nb	<0.1		0.12	0.1	<0.01		<0.05	
Cs	<0.1		<0.1		<0.01		<0.1	
Ba	153		10.8	3.7	6.18	1.31	1.54	2.1
La	5758		7.73	5.1	0.09	0.11	<0.04	
Ce	15222		20.7	16.5	0.24	0.29	<0.05	
Pr	1181		3.38	4.7	0.03	0.04	<0.04	
Nd	3716		5.80	4.0	0.07	0.20	<0.02	
Sm	493		1.45	1.2	0.09	0.08	<0.3	
Eu	54		0.22	0.1	0.09	0.03	<0.06	
Gd	277		0.69	0.5	0.06	0.09	<0.3	
Tb	30.7		0.14	0.2	0.02	0.02	<0.05	
Dy	136		0.55	0.3	0.31	0.15	<0.2	
Ho	19.9		0.11	0.2	0.05	0.05	<0.03	
Er	42		0.13	0.1	0.27	0.08	<0.1	
Tm	3.5		0.01	0.02	0.03	0.03	<0.04	
Yb	46		0.05	0.08	0.18	0.14	<0.2	
Lu	1.5		<0.03		0.02	2.00	<0.04	
Hf	227		0.21	0.2	0.01	0.02	<0.2	
Ta	<0.1		0.17	0.1	<0.01		<0.15	
Pb	<0.2		<0.12		<0.15		<0.2	
Th	2807		10.5	9.5	<.05		<0.04	
U	443		2.35	1.2	0.04	0.01	<0.04	

FIGURE 4. Hibonite-grossite aggregates. (**a**) Large grain of hibonite-grossite aggregate with millimeter-size spheres of native V (V^0). (**b**) Transmitted-light photo of the transparent specimen, enclosing black spinel grain and rods of V^0. (**c**) Phase map of **b** showing paragenesis of aggregates. Comparison of **b** and **c** shows that each tiny V^0 inclusion represents the end of a long rod or dendrite branch. (Color online.)

FIGURE 5. Hibonite-grossite aggregate is illustrating crystallization sequence. (**a–e**) Resorbed corundum in hibonite reflects peritectic reaction L + Cor → Hib, followed by grossite + spinel ± krotite; fluorite and $Ca_4Al_6F_2O_{12}$ crystallize last. V^0 appears to separate from the melt at temperatures near the peritectic reaction, as few inclusions of V^0 are found in the corundum. (**f**) Aggregate showing late crystallization of the F-bearing perovskite phase. (**g–h**) BSE image and phase distribution map showing intergrowth of perovskite and fluorite. Dark gray phase in BSE image is gibbsite, which replaces fluorite and leaves geode-like open cavities. (Color online.)
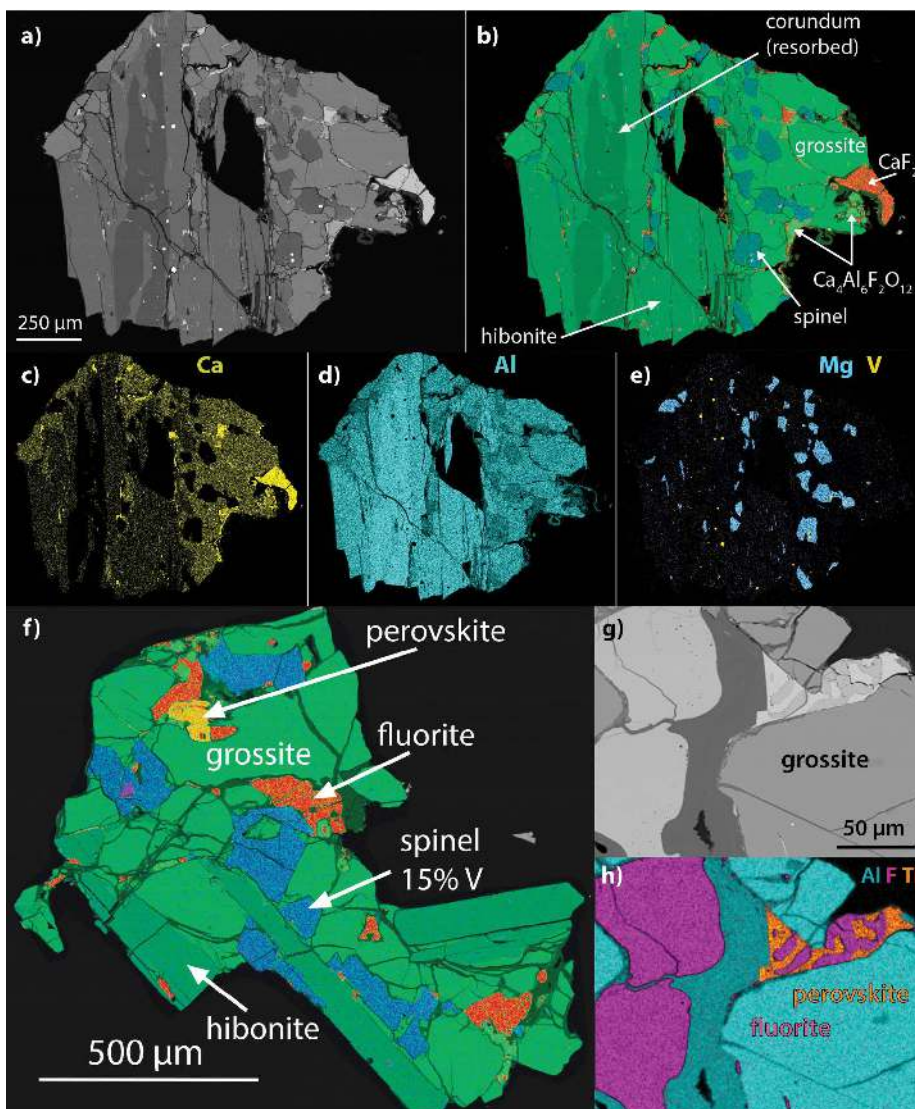
excess of Al. This feature is common to spinels in the less-evolved melt pockets without hibonite (our unpublished data), suggesting that either Ti or Al substitutes for Mg, but it is not clear from the analyses how charge balance would be achieved. Spinels in the

hibonite-grossite aggregates (paragenesis B) show a range of compositions, related to the presence of native V. Spinels in aggregates with no visible V^0 contain 9–16 wt% V (4.5–8 at%), and 1.7–8% wt% Mn; with a few exceptions, the contents of V and
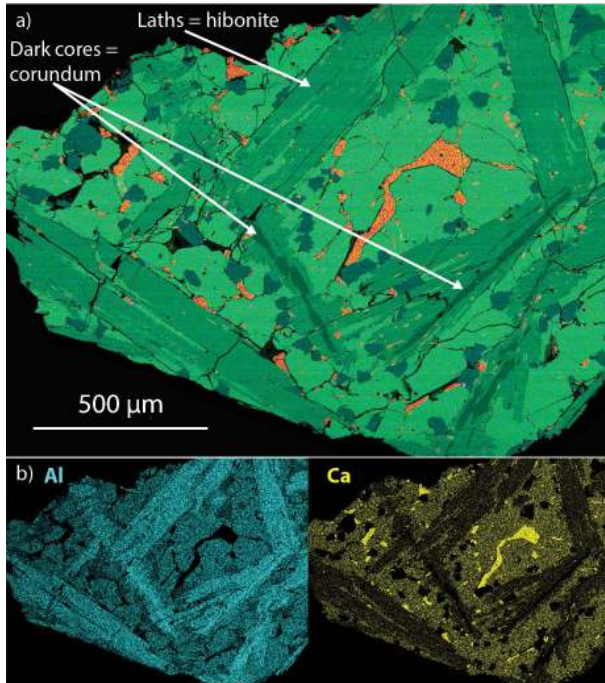
FIGURE 6. (**a**) Phase map of aggregate showing randomly oriented hibonite plates, with narrow resorbed corundum cores, and hibonite+grossite intergrowths at edges of plates. Grossite (light green) is euhedral against CaF_2 (orange), the last phase to crystallize. Spinels (blue-green) are euhedral. (**b**) Element-distribution maps for Ca and Al. (Color online.)

Mn are positively correlated, while both MgO and Al_2O_3 show negative correlations with V_2O_3 (Supplemental[1] Fig. S4). Detailed studies of the related phase dellagiustaite (ideally AlV_2O_4; Cámara et al. 2018, 2019), show all vanadium is ordered in the octahedral sites, with Al in the tetrahedral site; $^AAl^B(V^{2+}V^{3+})O_4$ (where A are tetrahedral sites and B are octahedral sites). It seems likely that this is also the case in the high-V spinels reported here.

Spinels in aggregates with scattered small beads of V^0 contain 2–5 wt% V and 0.3–1.3 wt% Mn. In aggregates with abundant V^0, the spinels mostly contain <0.5 wt% V and Mn. These less V-rich spinels have 2.0 Al ions per formula unit, suggesting that all of the V substitutes for Mg.

The Ca-Al oxyfluoride in the hibonite-grossite-spinel aggregates (Figs. 5 and 6) has the formula $Ca_4Al_6O_{12}F_2$; it is known from experimental studies on the CaO-Al_2O_3-F system (Kim 2011). F. Cámara, R. Pagano, A. Pagano, L. Bindi, and F. Nestola have described this phase in similar material from Sierra de Comechingones, San Luis, Argentina, and have proposed the name calfidine (IMF proposal number 2018-093; not yet approved).

All EDS analyses of fluorite contain carbon and may fit a formula $CaF_{2-x}C_x$. The EMP analyses did not include carbon, but the deficiency in the sums suggests the presence of a missing component such as carbon.

The perovskite phase has the formula $CaTiO_3$, implying that the Ti is present as Ti^{4+}, this is anomalous at the f_{O_2} implied by its coexistence with V^0. It also contains 1.6 wt% V and 1.3 wt% F.

The only Zr-Ti oxide grain large enough to analyze by EMP (Fig. 3) contains minor amounts of Al, Mn, Mg, and Ca; the structural formula of the mean analysis (Supplemental[1] Table S1) can be simplified as Zr_3TiO_8, implying that Ti is present as Ti^{4+}. However,
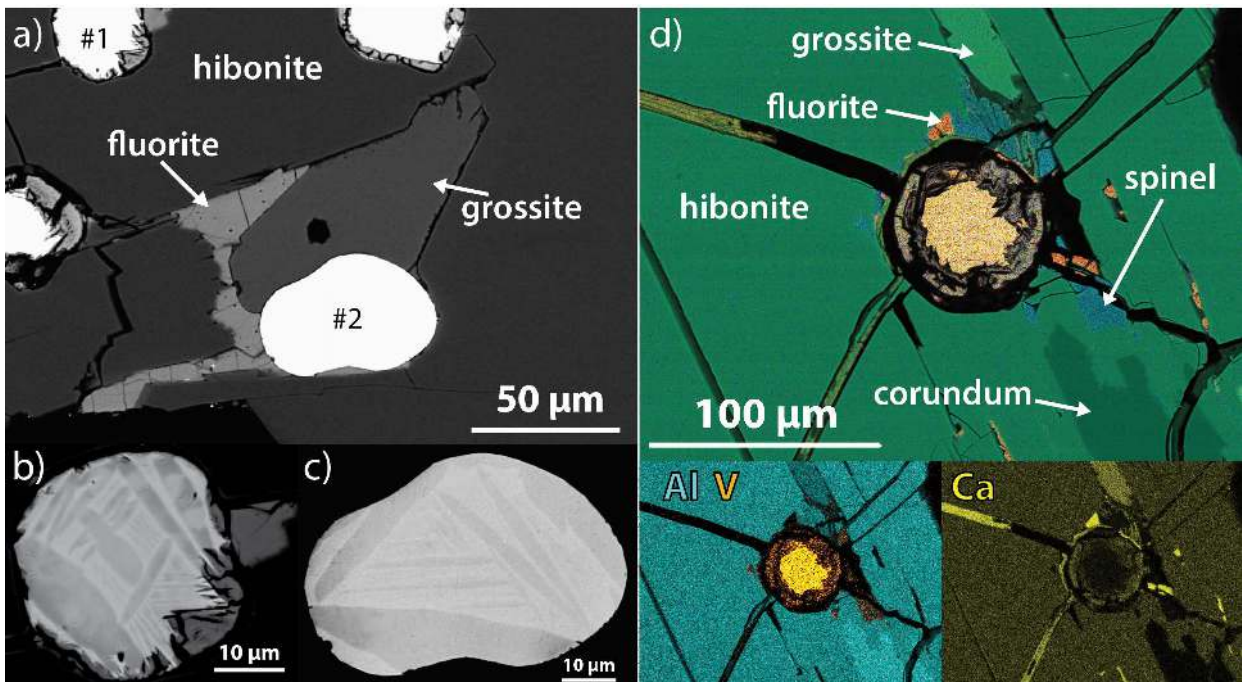

FIGURE 7. Parageneses of vanadium "balls." (**a**) Vanadium spheroids with spinel, grossite, and fluorite. (**b**) BSE image of spheroid 1 in **a**, showing intergrowth of Mn-rich and Mn-poor V. (**c**) BSE image and map of V distribution in spheroid 2 in **a**, showing intergrowth of native V with V-Mn alloy. (**d**) V spheroid partially altered to unidentified Ca-V phase(s). (Color online.)
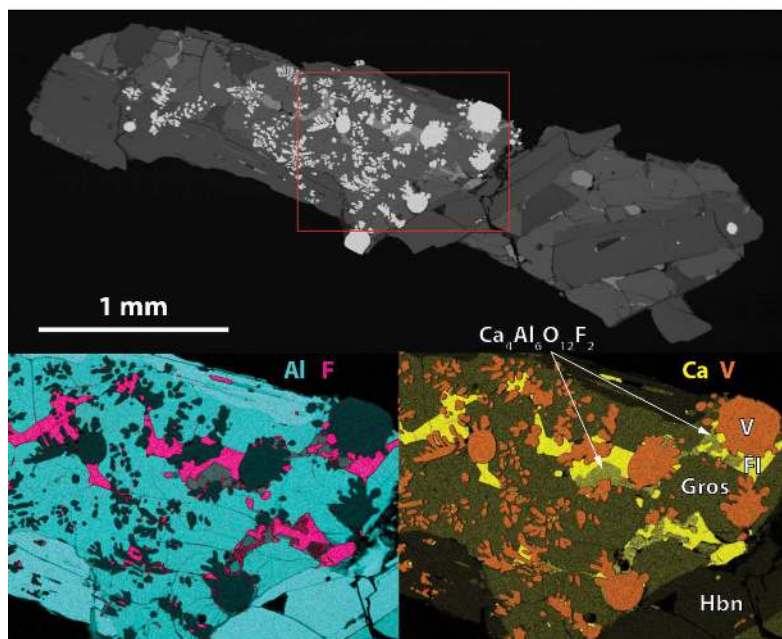
FIGURE 8. High-Al (mean 15 wt%) V balls in a nest of grossite between hibonite laths, with outlines suggesting they were fluid when trapped. Note euhedral $Ca_4Al_6O_{12}F_2$ is protruding into fluorite, the last phase to crystallize. The coexistence of $Ca_4Al_6O_{12}F_2$ with grossite and fluorite constrains the crystallization of the assemblage to >1150 °C (Kim 2011); see Supplemental[1] Figure S5. (Color online.)
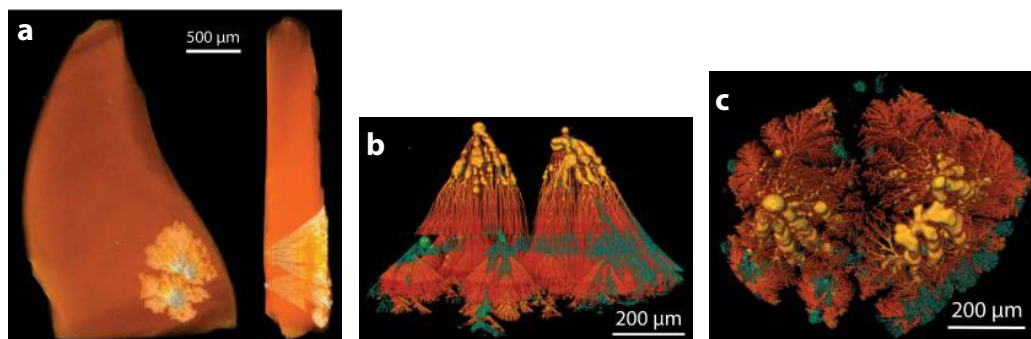

FIGURE 9. 3D-μCT images of dendritic native V in hibonite. (**a**) A low-resolution image of two dendrite clusters in a hibonite grain. (**b**) Magnified view, looking parallel to (0001) face; red to orange = vanadium; green = open cavities. (**c**) View from starting point, toward crystal face along *c* axis. Tendrils radiate off irregular clumps of V^0. Some consist of a series of joined balls that extend toward the crystal surface, then sprout into 3D dendritic networks with clear breaks and restarts at intermediate crystal planes. The patterns suggest nucleation of V melts on the surface of growing crystals. (See animated version in Supplemental[1] Fig. S3.) (Color online.)

the large standard deviations on the mean analysis indicate that this "phase" is very heterogeneous. Multiple SEM-EDS analyses that sample smaller volumes (Supplemental[1] Table S1) suggest the presence of several other oxides with variable ratios of (Zr+Ti)/O in which Ti appears to be present as Ti^{3+}. These may represent breakdown products of the Zr_3TiO_8 phase shown in Figure 3, but most occur as discrete grains. Further TEM studies will be required to confirm the nature of these phases.

The smallest vanadium spheres are nearly pure V^0, with 0.5–2 wt% Si and 1.5–2.5 wt% Mn. As these are inclusions are in hibonite or corundum, the Si is assumed to substitute in the alloy, rather than being a matrix contamination. Most larger V inclusions have lower Si, but contain 1–2% Cr and 0.5–3.5% Mn, and may have

up to ca. 4 wt% Al (V_9Al; Supplemental[1] Table S1; Fig. 9). The latest to form are irregular balls with drop-like protruberances that occur in nests of grossite surrounded by laths of hibonite (Fig. 8). These are similar in form to the drops that develop into the spectacular dendrites (Figs. 9, Supplemental[1] S3). They contain even higher levels of Al, with up to 15 wt% and a mean of 12% (V_4Al; Supplemental[1] Table S1); single-crystal XRD has confirmed a cubic structure (L. Bindi, pers. comm., August 2018).

Trace elements

Mean trace-element data for the major phases, from LA-ICP-MS analysis, are given in Supplemental[1] Table S2 and shown in Figure 10.

Brought to you by | Macquarie University
American Mineralogist, vol. 104, 2019
Authenticated | bill.griffin@mq.edu.au author's copy
Download Date | 2/4/19 12:40 AM

Hibonite in the corundum aggregates (paragenesis A) is extremely enriched in the REE (ΣREE = 2.7 wt%) with a moderate enrichment in LREE over HREE. It shows small negative anomalies in Sr, Eu, and Y, and it shows a positive anomaly in Yb. Ti reaches 1.7 wt%, Sr 1 wt%, and Zr 0.35 wt%. Th + U are also enriched (0.3 and 0.04 wt%), while vanadium is very low (2 ppm). Fe is absent, although minor Mn (34 ppm) is present; the only other transition element is Ni (3.5 ppm).

Hibonite in the hibonite-grossite aggregates (paragenesis B) shows LREE enrichment and a mild depletion in HREE relative to chondrites; Ba is depleted relative to Ce and La. The extended REE pattern is essentially parallel to that of the mean hibonite in paragenesis A (Fig. 10b), but lower in most elements by about two orders of magnitude and shows a relative depletion in Zr. One grain (982-2c-01) shows an unusual depletion in the lighter elements (Sr to Ce, Ba) while the other REE levels are similar to those in the mean hibonite. Most grains show negative Eu anomalies (Eu/Eu* = 0.2–0.82, mean 0.46, n = 9), but the other

anomalies seen in the interstitial-hibonite pattern are absent. Ti contents in the hibonites of paragenesis B range from 70–720 ppm, and are roughly correlated with V contents, which range from 1100–13 300 ppm. The highest V contents are found in grains with small inclusions of V^0, although care was taken to avoid these during analysis. The next most abundant transition element is Mn (50–580 ppm) and most grains carry low levels of Fe and/or Cr. Th and U contents are scattered (1–17 ppm and 1.4–4 ppm, respectively), but Th/U ratios show less spread [3.8 ± 2.1(1σ)]. Most Na values are around 20 ppm, but K is <0.02 wt% in most grains. B is reported at levels of 20–50 ppm (but is <2 ppm in one); we cannot be confident of these values, but note that the Mt Carmel system does contain boride minerals (TiB_2; Griffin et al. 2016).

Grossite in paragenesis B has generally chondritic to sub-chondritic levels of the REE, and low levels of most other trace elements (Fig. 10c). The high standard deviations relative to the absolute values suggest that many of these elements reside in tiny inclusions of other minerals, or melt, inside the grossite. Most grains show a pattern with relatively flat HREE and MREE, and depleted LREE; the patterns and absolute abundances of Y and the HREE are similar to those of coexisting hibonite (Figs. 10b and 10c). However, some grains do not show the LREE depletion. Ba is elevated relative to La and Ce, and all grains show high levels of Sr and Y compared to the MREE, although the absolute levels are similar to those in hibonite. In contrast to the hibonite, most grains of grossite show a small positive Eu anomaly. Ti (30–120 ppm) contents are lower than in hibonite, but contents of V (850–2750 ppm) and Mn (0–510 ppm) overlap the ranges seen in hibonite, and Fe levels (mostly 100–250 ppm) are higher. There is no obvious correlation between Ti and V. In marked contrast to the hibonites, contents of Th and U in grossite are typically <0.05 ppm.

Large spinel grains in paragenesis B contain ~2.5% V; Mn contents range from 3100–6400 ppm, while Cr, Ti, and Zn values average 77, 150, and 10 ppm, respectively. Ga contents are <0.2 ppm, giving very high Al/Ga ratios. Ca contents are unusually high for spinels, at 1100–4300 ppm.

A single LA-ICP-MS analysis of a large vanadium sphere in hibonite gave values of 490 ppm Zn, 21 ppm Cu, and 69 ppm Nb.
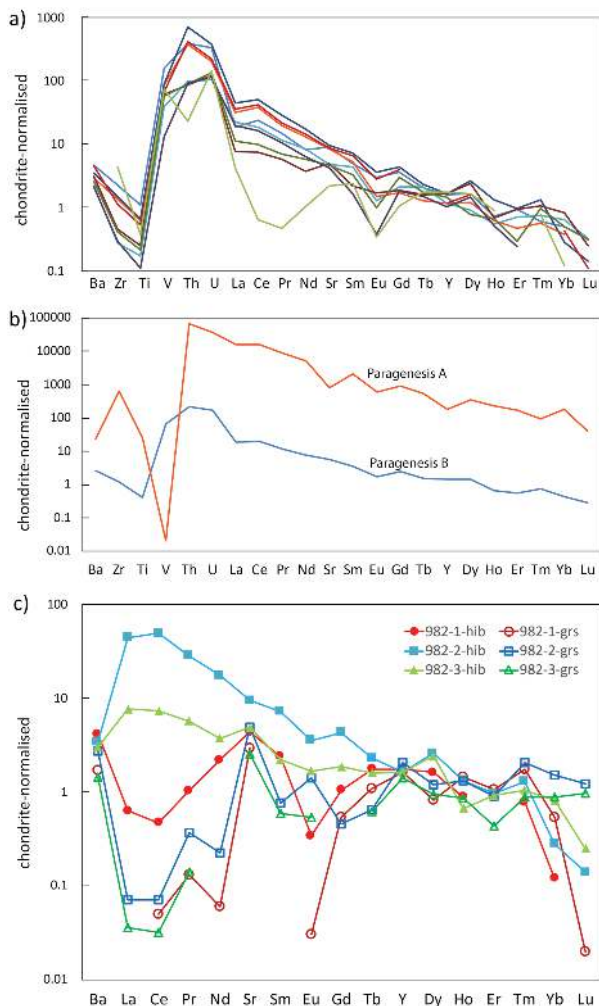
DISCUSSION

Conditions of formation

Temperature. The temperatures during the crystallization of the Mt Carmel super-reduced assemblages can be estimated from experimental data, which are mainly from 1-atm experiments. Therefore the estimated temperatures may represent minimum values in the individual simple systems. The major phases all lie within the simple and well-studied system $CaO-MgO-Al_2O_3-SiO_2$; the coexisting melts consist mainly of these oxides, though with significant levels of Ti, Zr, and REE.

Hibonite crystallizes from $CaO-Al_2O_3$ melts (Fig. 11a) via the peritectic reaction Crn + Liq → hibonite; different experimental or theoretical studies place this reaction at 1850–1880 °C; in more SiO_2-rich systems (Fig. 12) the peritectic extends down to ca. 1475 °C. There is disagreement in the literature as to the nature of lower-temperature phase transitions on this binary. Some studies (e.g., Guo et al. 2015; Azof et al. 2017) show both
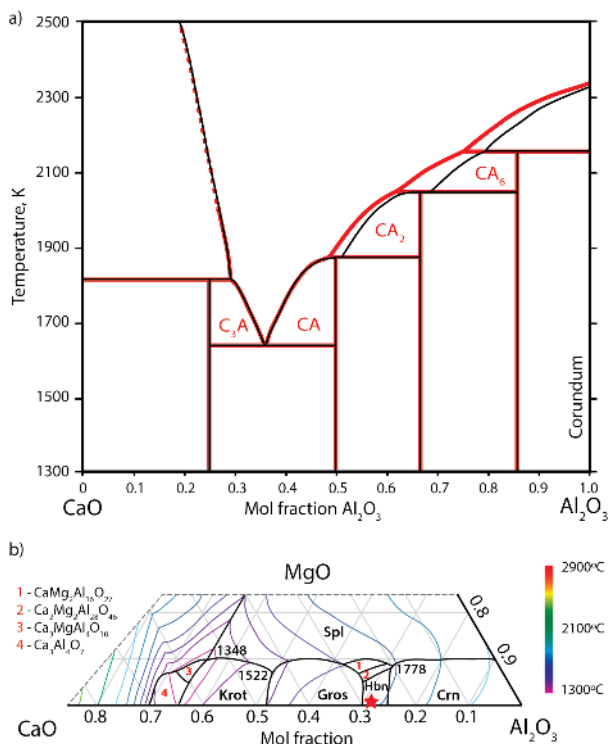
FIGURE 10. Chondrite-normalized trace-element abundances. (**a**) Hibonite in hibonite-grossite aggregates. (**b**) Mean hibonite in aggregates vs. mean hibonite included in corundum. (**c**) Coexisting hibonite-grossite pairs, linked by color. (Color online.)

FIGURE 11. Phase diagrams constraining temperatures of crystallization. (**a**) Two "end-member" versions of the CaO-Al$_2$O$_3$ binary, showing reactions as eutectics (Guo et al. 2015; black lines) or peritectics (Jerebtsov and Mikhailov 2001; red lines); red star shows the average bulk composition of hibonite-grossite aggregates (Supplemental[1] Table S2). (**b**) Al-corner of CaO-MgO-Al$_2$O$_3$ liquidus diagram (after data from FactSage); intermediate Ca-Mg-Al oxides (1–4) have not been identified in this study. (Color online.)

FIGURE 12. CaO-Al$_2$O$_3$-SiO$_2$ liquidus diagram at 1 atm. pressure (after Osborn and Muan 1960; Gentile and Foster 1963), showing compositions of hibonite-grossite-spinel aggregates, and calculated and analyzed melts; red arrows show the effects of desilication, and crystallization of hibonite+grossite aggregates. (Color online.)

grossite and krotite melting congruently, producing the binary eutectics Hbn + Gros + Liq and Gros + Krot + Liq. Others (e.g., Mao et al. 2004) show both phases melting incongruently, in peritectic reactions Hbn → Gros + Liq and Gros → Krot + Liq. Still, others show singularities in which the peritectic reactions correspond to the congruent melting points of grossite and krotite, respectively. The older experimental work is more consistent with the modeling of Mao et al. (2004; Fig. 12). In the aggregates of Paragenesis B, there is no obvious reaction relationship between hibonite and grossite, but the grossite + spinel assemblage does appear to crystallize after hibonite.

Grossite (Gros) appears at 1750–1780 °C in the binary system, and krotite at ca. 1600 °C. In the 1 atm CaO-MgO-Al$_2$O$_3$ system (Fig. 11c), the Hbn + Gros + Liq peritectic descends to the Gros + Spl + Liq cotectic at ca. 1690 °C. In the 1-atm liquidus diagram two intermediate Ca-Al-Mg oxides appear through peritectic reactions just above this temperature (Fig. 11b), but these phases have not been recognized in the Mt Carmel system. Their apparent absence may be a pressure effect (see below), or it may reflect the presence of abundant fluorine in the system, effectively sequestering Ca. Alternatively, they may have been consumed in peritectic reactions. The presence of krotite as an interstitial late phase implies that the residual melts evolved
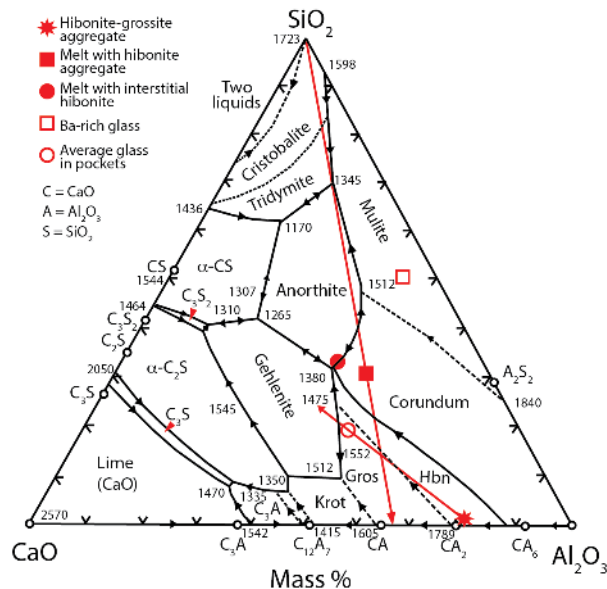
further, toward the peritectic Gros + Liq (±spinel) → krotite at ca. 1520 °C (Fig. 11b). Krotite + Spn + Liq coexist along a cotectic leading to more Ca-rich compositions, not seen in our samples, at ca. 1350 °C.

The presence of fluorine may lower these liquidus temperatures. The fluorite-grossite assemblage precipitates at ca. 1375 °C in the 1-atm CaF$_2$-CaAl$_2$O$_4$ system and the Ca$_4$Al$_6$O$_{12}$F$_2$ phase crystallizes from ca. 1480 °C to a eutectic with fluorite at 1375 °C (Supplemental[1] Fig. S5; Kim 2011). Ca$_4$Al$_6$O$_{12}$F$_2$ is unstable at T <1150 °C, providing a lower limit for the cooling of the system before eruption terminated the evolution of the melts. The presence of this phase implies that F^{1-} had replaced a significant amount of the O^{2-} in the melt (Peng et al. 2012).

One spinel has been found coexisting with hibonite in the melt pockets (Supplemental[1] Table S1). Like spinels coexisting with tistarite and the TAZ phase in the earlier stages of the melt evolution, it has a large excess of Al$_2$O$_3$ and a deficit in divalent cations; by comparison with the experimental MgO-Al$_2$O$_3$ system (e.g., Bhaduri and Bhaduri 1999; Callister 2007) it gives a T close to 1400 °C, within the range of temperatures derived from spinels in other melt pockets (1600 to 1200 °C, with a mean of 1400 °C; our unpublished data). In contrast, the spinels in the hibonite-grossite aggregates are nearly stoichiometric (Mg,V)Al$_2$O$_4$, which yields a temperature around 1200 °C.

Pressure. There are no independent constraints on the pressure of formation for the hibonite-grossite assemblage; it crystallized at very low pressure in the Solar nebula (Beckett et al. 2006), at ca. 1–2 km depth in the Hatrurim Formation (Gross 1977), and at ca. 10–30 km depths in the granulite-facies occurrences (Rakotondrazafy et al. 1996). Dmisteinbergite, the metastable high-T hexagonal polymorph of anorthite, occurs as

Brought to you by | Macquarie University
Authenticated | bill.griffin@mq.edu.au author's copy
Download Date | 2/4/19 12:40 AM
American Mineralogist, vol. 104, 2019

a quench phase in many melt pockets (Xiong et al. 2017). In experiments, this phase can be produced by rapid cooling of the melt to ca. 1200 °C (Davis and Tuttle 1952). In the present case, this reflects the peritectic reaction Crn + Liq → An, which is constrained experimentally to $P_{min} > 0.9$ GPa and T ca. 1450 °C (Goldsmith 1980). The parageneses in the hibonite-grossite aggregates (Figs. 5 and 6) document crystallization across the peritectic Liq + Crn → hibonite, followed by crystallization along the hibonite-grossite cotectic to where it joins the cotectic Gros + Spl + Liq. Ottonello et al. (2013) modeled the $CaO-Al_2O_3-SiO_2$ liquidus at pressures to 2 GPa and argued that grossite is not a liquidus phase at $P \geq 1$ GPa (Fig. 13). The presence of $CaAl_2O_4$ as krotite, rather than the higher-P polymorph dmitryivanovite, also limits P to <2 GPa (Mikouchi et al. 2009). If these constraints are accepted, the Mt Carmel corundum-SiC system was crystallizing at $P = $ ca. 1 GPa (depths of 25–30 km) near the crust-mantle boundary in the area (Segev and Rybakov 2011), when the host basalts erupted.

Oxygen fugacity (f_{O_2}). Hibonite is stable over a wide range of oxygen fugacity. The Mt Carmel assemblages described here require very reducing conditions, consistent with the occurrence of tistarite (Ti_2O_3) and SiC as inclusions in corundum. The presence of a positive Yb anomaly in the hibonite of paragenesis A is consistent with this low f_{O_2}, as Yb^{2+} will substitute for Ca in the hibonite more readily than Yb^{3+}. In the hibonite-grossite aggregates of paragenesis B, the coexistence of native V requires $f_{O_2} < \Delta IW-8$ (Fig. 1). As noted above, low oxygen fugacity is not a pre-requisite for the crystallization of the hibonite-grossite-spinel assemblage. However, it was the progressive lowering of f_{O_2} during the evolution of the magmatic system that led to the immiscibility of silicide melts, driving the desilication of the magma that ultimately allowed the crystallization of the oxide assemblage hibonite-grossite-spinel (Griffin et al. 2016; Xiong et al. 2017).

In summary, the crystallization of the hibonite-grossite assemblage in the Mt Carmel system probably occurred at depths of 25–30 km, temperatures falling from ca. 1500 °C to ca. 1200 °C prior to the eruption, and f_{O_2} between $\Delta IW-6$ and $\Delta IW-9$.

Melt evolution

For a rough estimate of the composition of the bulk crystallization products, element maps of eight hibonite-grossite aggregates were point-counted to determine the modal abundances of the analyzed phases, and bulk compositions were calculated. These proved to show little variation in composition (Table 1); the mean contains ca. 80 wt% Al_2O_3, 16 wt% CaO, 2 wt% MgO, and 1 wt% F, while other components are present at levels of ≤0.5%. This composition lies close to the hibonite-grossite boundary on the CA binary (Fig. 11a), and the CAS ternary plot (Fig. 12), but in the field of corundum in the CMA ternary (Fig. 11b).

The major-element composition of a melt coexisting with the average hibonite in paragenesis A (24 analyses) was calculated using the D values of Kennedy et al. (1994), based on 1-atm experimental studies, and our own values derived from a single hibonite-glass pair (Fig. 2). There are obvious hurdles in this approach, in terms of concentration levels and non-ideality of melts, but the data may be useful on a comparative basis. The value for $D_{Si}^{h/m}$ given by Kennedy et al. (1994) is clearly not applicable to
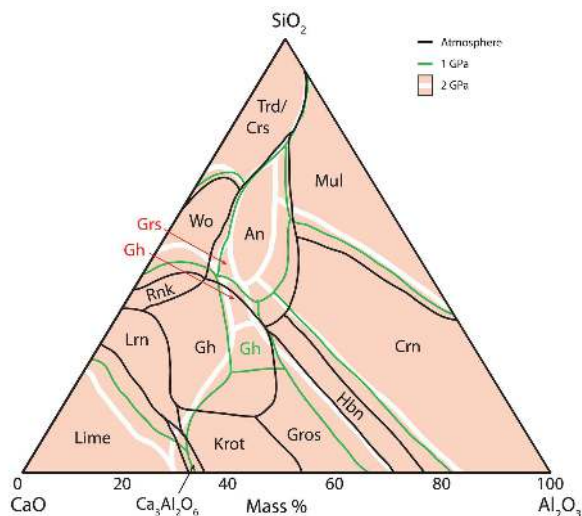

FIGURE 13. Calculated liquidus diagrams of the $CaO-Al_2O_3-SiO_2$ system at 3 pressures, after Ottonello et al. (2013). Trd/Cr = tridymite/cristobalite; Qz = quartz; Wo = wollastonite; An = anorthite; Mul = mullite; Rk = rankinite; Gh = gehlenite; Crn = corundum; Hbn = hibonite; Gros = grossite, Grs = grossular; Krt = krotite; Lrn = larnite. Note the shrinkage of the fields of anorthite and gehlenite, and the expansion of the krotite and hibonite fields, with increasing P, and disappearance of the liquidus field of grossite above ~1 GPa. (Color online.)

the Mt Carmel material, as it would predict >100 wt% SiO_2 in the melt. A value for $D_{Si}^{h/m}$ derived from our analysis of the glass coexisting with one hibonite in corundum would predict 28 wt% SiO_2 in the melt coexisting with the mean interstitial hibonite. The actual analyzed melt contains 38.3 wt% SiO_2, while the interstitial hibonite coexisting with it has higher SiO_2 than the mean value.

As expected, the melt predicted using both approaches is very high in Al_2O_3 and CaO (Supplemental[1] Table S2). MgO contents predicted by the data of Kennedy et al. (1994) are higher than our calculated values. The levels of Zr and Ti predicted by both sets of distribution coefficients are similar. This composition lies near the corundum-anorthite cotectic on the $CaO-Al_2O_3-SiO_2$ (CAS) liquidus phase diagram at 1 atm pressure (Fig. 12), but close to the corundum-hibonite peritectic at 1 GPa (Fig. 13; Ottonello et al. 2013). Glasses coexisting with hibonite in meteoritic spherules, interpreted as melts condensed from the solar nebula (Ireland et al. 1991) are broadly similar in being essentially CMAS melts but have lower Al and higher Si, Ca, and Mg than those calculated for the interstitial hibonite.

The calculated major-element composition of the melt in equilibrium with the mean hibonite composition of paragenesis B (Supplemental[1] Table S2) suggests a further evolution to higher CaO/Al_2O_3, but lower MgO. SiO_2 and TiO_2 are below detection limits in the hibonite, and this may suggest SiO_2 contents ≤20 wt% and TiO_2 contents ≤0.5 wt% in the melt. This composition, though poorly constrained, lies within the CAS liquidus field of corundum at 1 atm and at 1 GPa (Figs. 12 and 13).

If the melts calculated for the two parageneses are linked by the evolution of the trapped melts beyond the corundum-hibonite peritectic, then evolution is unlikely to have been driven only

by fractional crystallization of the observed assemblages, which would increase SiO_2 but decrease Al_2O_3 in the melt. However, such an evolution would be broadly consistent with the overall trend is seen in the Mt Carmel system, of continued desilication of the silicate melts by immiscible separation of silicide melts and crystallization of SiC, with falling f_{O_2} (Fig. 13).

The Fe-Ti silicide melts that separated from the parental melts earlier in their evolution contain <0.5 wt% V (our unpublished data), suggesting that V did not partition strongly into the metallic melts. This is consistent with the generally lithophile nature of V, and the observation that the partition coefficient $D_V^{metallic\ melt/silicate\ melt}$ decreases (i.e., V becomes more lithophile) with increasing Si content in the metallic melt (Tuff et al. 2011). However, $D_V^{metallic\ melt/silicate\ melt}$ should be higher at low f_{O_2}; this may indicate that most of the separation of silicide melts occurred at high enough f_{O_2} (ΔIW-6 to ΔIW-7) to hinder a stronger uptake of V, leaving enhanced levels of V in the residual melts.

During the further evolution of the melts, there were few crystallizing phases that accepted significant levels of V, until the appearance of the hibonite-related spinels described here. At that point, f_{O_2} may have been low enough for the stability of both V^{3+} and V^{2+}, allowing substitution for Mg and Al in the first spinels, up to 8 at% (Supplemental[1] Table S1). XANES analysis of V in fassaitic pyroxenes from refractory CAIs has found V^{2+}/V^{tot} ratios as high as 0.7, consistent with a solar gas (i.e., H-dominated; Simon et al. 2007). The presence of Ti^{2+}-bearing phases (e.g., TiC) and V^0 suggest that the minimum f_{O_2} during the late stages of the Mt Carmel system was at least this low (Fig. 1), and thus that H_2 may have been the main volatile species present.

Righter et al. (2006; see also Papike et al. 2013) studied the partitioning of V between silicate melts and Al-spinels over a wide range of oxygen fugacity and composition. Using their Equation 2 and the constants they calculated from the low-f_{O_2} experiments, we estimate $D_V^{spinel/silicate\ melt}$ to be in the range of 43–45 for the spinels in the hibonite-grossite aggregates. This approach suggests that the melt coexisting with the high-V spinels (Supplemental[1] Table S1) contained on the order of 1000–1500 ppm V. The concentration of V in the late Ca-Al-Si-O melts thus represents only a moderate (5×) enrichment relative to a proposed mafic parental melt (200–300 ppm; Fig. 2). The melt that crystallized the medium-V spinels contained about 400 ppm V, and the melt with the low-V spinels, which crystallized in the presence of V^0, contained only about 35 ppm V. This trend partly reflects the rapid sequestration of V into its own melt phase, which is clearly immiscible with the silicate melt.

Composition of coexisting melts: Trace elements

The $D^{hibonite/melt}$ values for a range of trace-elements published by Kennedy et al. (1994; K94 below), Ireland et al. (1991; I91 below), and Drake and Boynton (1988; DB88 below) allow the calculation of the trace-element patterns of the melts that would have equilibrated with the analyzed hibonites (Fig. 14a; Supplemental[1] Table S2). The melts calculated from the interstitial hibbonites in the corundum aggregates (paragenesis A) have relatively flat HREE-MREE and mild enrichment in the LREE. The LREE patterns calculated with I91 have lower MREE-HREE than those calculated from the K94 data. The D_{Eu} value of K94 is >1 and produces a negative Eu anomaly,

whereas those of I91 and DB88 produce positive Eu anomalies. The three sets of D_{Yb} values all produce a marked positive Yb anomaly in the melts with the interstitial hibonite of paragenesis A. The calculated melts have much higher contents of the REE and other trace elements than melts coexisting with hibonite in meteoritic glass spherules (Ireland et al. 1991; Fig. 14c). However, the meteoritic glasses do not show LREE enrichment, nor any Yb anomaly.

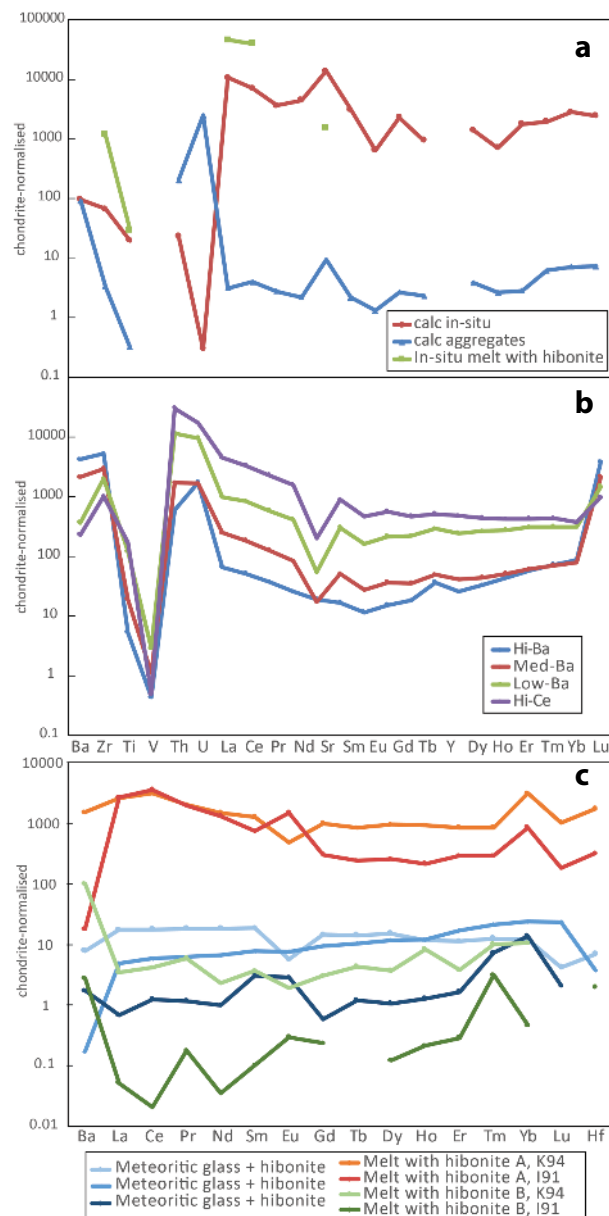The calculated melts in equilibrium with the hibonite of

Figure 14. Analyzed glasses and calculated melts. (**a**) Trace-element spectra of melts calculated using distribution coefficients of Kennedy et al. (1994; K94), and the analyzed glass coexisting with hibonite in Paragenesis A. (**b**) Trace-element spectra of glasses described in text. (**c**) Comparison of calculated melts with hibonite-bearing glasses from Lance and Murchison meteorites (Ireland et al. 1991). (Color online.)

paragenesis B are, as might be expected, much more depleted in most trace elements (except Th, U, and Ba), in general rougher (a function of low count rates) and more spoon-shaped than the pattern of the paragenesis A melt. The melts calculated from the hibonite of paragenesis B have REE levels similar to those of meteoritic glasses, but the patterns are more spoon-shaped than those of the meteoritic glasses.

LA-ICP-MS analyses of glasses in the melt pockets in the corundum aggregates define three prominent populations, ranging from a high-Ce, low-Ba type to a lower-Ce, higher-Ba type (Fig. 14b; Supplemental[1] Table S2); all three types have strongly negative Sr anomalies. While the high-Ce glasses have flat HREE-MREE and LREE-enrichment, the lower-Ce glasses have a more concave-upward pattern. The higher-Ce, lower-Ba glasses are broadly similar to the calculated melt in equilibrium with the interstitial hibonites (paragenesis A). In the pyroclastic ejecta, many fragments of the corundum aggregates are coated in the low-Ce, high-Ba glass, which has patterns even more upward-concave than those of the higher-Ce glasses (Fig. 14b). These glasses are broadly similar to the calculated melt in equilibrium with the mean hibonite of paragenesis B, but also show many differences.

For comparison with the partitioning data of Kennedy et al. (1994), Ireland et al. (1991), and Drake and Boynton (1988), we have calculated the distribution coefficients between the interstitial hibonites (paragenesis A) and the high-Ce, low-Ba glass, and between the aggregate hibonites (paragenesis B) and the low-REE, high-Ba glasses (Supplemental[1] Table S2). The D values calculated from the interstitial hibonite vs. the high-Ce glasses in general agree within a factor of 2 with those of I91 and DB88. Notable exceptions are D_{Sr}, D_V, D_{Zr}, and D_{Ba}; for the latter two the K94 D values look more appropriate. The D values proposed here may be useful in further studies of meteoritic hibonite associations, especially for elements where no D values are otherwise available. The D values calculated by pairing the hibonite of paragenesis B with the high-Ba glass do not provide a good match with any of the other data sets, suggesting that the high-Ba glass, although apparently formed late in the magmatic evolution, was not in equilibrium with the hibonite-grossite-spinel aggregates.

SUMMARY

(1) The assemblage hibonite + grossite + spinel of paragenesis A crystallized from evolved, FeO-free, highly reduced silicate melts trapped within aggregates of hopper/skeletal corundum, found as ejecta in the late Cretaceous mafic-ultramafic explosive-pyroclastic volcanic rocks exposed on Mt Carmel, N. Israel. Coexisting minerals indicate $f_{O_2} \leq \Delta IW-6$. These highly reducing conditions are attributed to interaction between mantle-derived $CH_4 + H_2$ fluids and mafic magmas near the base of the crust (25–30 km).

(2) Coarse-grained aggregates of hibonite + grossite + spinel + fluorite ± krotite ± perovskite ± $Ca_4Al_6O_{12}F_2$ (paragenesis B) appear to represent the further evolution of the silicate melts. Textural evidence shows that hibonite crystallized via the peritectic reaction Crn + Liq → Hbn, and was succeeded by Hbn + Gros + Spl.

(3) Native vanadium occurs as rounded inclusions in the hibonite, grossite, and spinel of the coarse aggregates; some of these inclusions develop into spectacular dendritic clusters roughly parallel to the c axis of hibonite crystals. The presence

of V^0 requires $f_{O_2} \leq \Delta IW-9$, suggesting a decline in f_{O_2} by ~3 log units during the crystallization of this assemblage.

(4) Spinels in the hibonite + grossite +spinel aggregates contain 9–15 wt% V; those coexisting with minor V^0 contain 3–5 wt% V, and those coexisting with abundant V^0 contain ≤0.5 wt% V. In high-V spinels, vanadium appears to be present as both V^{2+} and V^{3+}, while in lower-Al spinels it may be present as V^{2+}; these spinels are essentially stoichiometric $(Mg,V)Al_2O_4$, and are consistent with crystallization temperatures around 1200 °C.

(5) The late crystallization of the previously unreported phase $Ca_4Al_6O_{12}F_2$ together with fluorite in the hibonite-grossite-spinel aggregates (paragenesis B) suggests that crystallization of the aggregates began at $T > 1400$ °C, cooled to the pseudo-eutectic Gros + Fl + $Ca_4Al_6O_{12}F_2$ + Liq at ca. 1375 °C, and remained at $T > 1150$ °C until crystallization was terminated by the volcanic eruption. This is consistent with the appearance of dmisteinbergite as a quench phase in melt pockets in corundum.

IMPLICATIONS

This is the first reported terrestrial example of the crystallization of hibonite and grossite from high-T silicate melts, the first terrestrial occurrence of krotite, and the first report of native vanadium melts. The Mt Carmel assemblages described here are analogous in many ways to those observed in many calcium-aluminum inclusions (CAI) inclusions in carbonaceous chondrites. The inferred conditions of crystallization of the Mt Carmel assemblages are similar to those of the CAIs in terms of temperature and f_{O_2}, but they appear to have formed at higher pressures, ca. 1 GPa. The analogies suggest that the Mt Carmel system also formed in the presence of abundant H_2 and carbon. These unusual mineral assemblages thus reflect a magmatic environment in which f_{O_2} was reduced to levels that imply coexistence with fluid phases dominated by hydrogen. Such environments have not previously been reported on Earth. Their existence suggests previously unrecognized processes, which may be widespread in connection with deep-seated magmatism (Griffin et al. 2018). The observations presented here emphasize the importance of immiscibility between silicate melts and metallic melts under conditions of low f_{O_2}, and this may be a significant factor in element fractionation and partial melting in a metal-saturated mantle. The depth(s) of origin of the CH_4-dominated volatile fluxes identified here remains to be determined, but the proposed transfer of such volatiles to shallow depths by deep-seated magmatism implies a deep source and may represent an underappreciated part of the deep carbon cycle

REFERENCES CITED

Apter, D.B. (2014) High pressure indicator minerals from the Rakefet magmatic complex (RMC), Mt Carmel, Israel. Abstracts Kimberley Diamond Symposium, Kimberley, South Africa.

Azof, F.I., Kolbeinsen, L., and Safarian, J. (2017) The leachability of calcium aluminate phases in slags for the extraction of alumina. Proceedings 35th International ICSOBA conference, Hamburg 2017, p. 243–253.

Beckett, J.R., Connolly, H.C., and Ebel, D.S. (2006) Chemical processes in igneous Calcium-Aluminum-rich inclusions: A mostly CMAS view of melting and crystallization. In D.S. Lauretta and H.Y. McSween, Eds., Meteorites and the Early Solar System II, pp. 389–429. University of Arizona Press.

Bhaduri, S., and Bhaduri, S. (1999) Phase and microstructural evolution of heat treated nanocrystalline powders in Al_2O_3-MgO binary system. Nanostructured Materials, 11(4), 469–476.

Callister, W.D.J. (2007) Materials Science and Engineering: An introduction (7th ed.). Wiley.

Cámara, F., Pagano, R., Pagano, A., and Bindi, L. (2018) Dellagiustaite. IMA 2017-101. CNMNC Newsletter No. 42, April 2018, page 446; Mineralogical Magazine, 82, 445–451.

Cámara, F., Bindi, L., Pagano, A., Pagano, R., Gain, S.E.M., and Griffin, W.L. (2019) Dellagiustaite: a novel natural spinel containing V^{2+}. Minerals, in press.

Curien, H., Guillemin, C., Orcel, J., and Steinberg, M. (1956) La hibonite, nouvelle espece minerale. Compte Rendu Academie Scientifique Paris, 242, 2845–2847 (in French).

Davis, G.L., and Tuttle, O.F. (1952) Two new crystalline phases of the anorthite composition, CaO. $Al_2O_3·_2SiO_2$. American Journal Science, Bowen, 250A, 107–114.

Drake, M.J., and Boynton, W.V. (1988) Partitioning of rare earth elements between hibonite and melt and implications for nebular condensation of the rare earth elements. Meteoritics, 23(1), 75–80.

Gentile, A.L., and Foster, W.R. (1963) Calcium hexaluminate and its stability relations in the system CaO-Al_2O_3-SiO_2. Journal American Ceramics Society, 46, 74–76.

Goldsmith, J.R. (1980) The melting and breakdown reactions of anorthite at high pressures and temperatures. American Mineralogist, 65, 272–284.

Griffin, W.L., Gain, S.E.M., Huang, J.X., Saunders, M., Toledo, V., Pearson, N.J., and O'Reilly, S.Y. (2016) First terrestrial occurrence of tistarite (Ti_2O_3): Ultra-low oxygen fugacity in the upper mantle beneath Mount Carmel, Israel. Geology, 44, 815–818.

Griffin, L.W., Huang, J.X., Thomassot, E., Gain, S.E.M., Toledo, V., and O'Reilly, S.Y. (2018) Super-reducing conditions in ancient and modern volcanic systems: Sources and behaviour of carbon-rich fluids in the lithospheric mantle. Mineralogy and Petrology, https://doi.org/10.1007/s00710-018-0575-x.

Griffin, W.L., Gain, S.E.M., Bindi, L., Toledo, V., Cámara, F., Saunders, M., and O'Reilly, S.Y. (2019) Carmeltazite, $ZrAl_2Ti_4O_{11}$, a new mineral trapped in corundum from volcanic rocks of Mt Carmel, northern Israel. Minerals, in press.

Gross, S. (1977) The Mineralogy of the Hatrurim Formation Israel. Geological Survey of Israel, 80 pp.

Grossman, J.N., Rubin, A.E., and MacPherson, G.J. (1988) ALH85085: a unique volatile-poor carbonaceous chondrite with possible implications for nebular fractionation processes. Earth and Planetary Science Letters, 91(1), 33–54.

Grossman, L., Beckett, J.R., Fedkin, A.V., Simon, S.B., and Ciesla, F.J. (2008) Redox conditions in the solar nebula: Observational, experimental, and theoretical constraints. Reviews in Mineralogy and Geochemistry, 68, 93–140.

Guo, C., Shang, S., Du, Z., Jablonski, P.D., Gao, M.C., and Liu, Z-K. (2015) Thermodynamic modeling of the CaO-CaF_2-Al_2O_3 system aided by first-principles calculations. CALPHAD, 48, 113–122.

Ireland, T.R., Fahey, A.J., and Zinner, E.K. (1991) Hibonite-bearing microspherules: A new type of refractory inclusions with large isotopic anomalies. Geochimica et Cosmochimica Acta, 55(1), 367–379.

Jerebtsov, D.A., and Mikhailov, G.G. (2001) Phase diagram of CAO-Al_2O_3 system. Ceramica International, 27, 25–28.

Kennedy, A.K., Lofgren, G.E., and Wasserburg, G.J. (1994) Trace-element partition coefficients for perovskite and hibonite in meteorite compositions. Chemical Geology, 117(1), 379–390.

Kim, D.-G. (2011) Experimental study and thermodynamic modelling of the CaO-SiO_2-Al_2O_3-CaF_2 system. Master thesis, McGill University Libraries.

Konovalenko, S.I., Ananyev, S.A., and Garmayeva, S.S. (2012) Rare and new minerals of the Tashelga-Maizaskaya zone of Gornaya Shoriya, their pecu-

liarities and nature. Journal of Siberian Federal Univeristy—Engineering and Technologies, 5, 301–310.

Kurat, G., Hoinkes, G., and Fredriksson, K. (1975) Zoned Ca-Al-rich chondrule in Bali: New evidence against the primordial condensation model. Earth and Planetary Science Letters, 26, 140–417.

Ma, C., Kampf, A.R., Connolly, H.C. Jr., Beckett, J.R., Rossman, G.R., Sweeney Smith, S.A., and Schrader, D.L. (2011) Krotite, $CaAl_2O_4$, a new refractory mineral from the NWA 1934 meteorite. American Mineralogist, 96, 709–715. https://doi.org/10.2138/am.2011.3693

Mao, H., Selleby, M., and Sundman, B. (2004) A re-evaluation of the liquid phases in the CaO-Al_2O_3 and MgO-Al_2O_3 systems. Computer Coupling of Phase Diagrams and Thermochemistry, 28, 307–312.

Mikouchi, T., Zolensky, M., Ivanova, M., Tachikawa, O., Komatsu, M., Le, L., and Gounelle, M. (2009) Dmitryivanovite: A new high-pressure calcium aluminum oxide from the Northwest Africa 470 CH3 chondrite characterized using electron backscatter diffraction analysis. American Mineralogist, 94, 746–750.

Osborn, E.F., and Muan, A. (1964) In E.M. Levin, C.R. Robbins, and H.F. McMurdie, Eds., Phase Diagrams for Ceramists, vol. 1, 219 pp. The American Ceramic Society, Columbus, Ohio.

Ottonello, G., Attene, M., Ameglio, D., Belmonte, D., Vetuschi Zuccolini, M., and Natali, M. (2013) Thermodynamic investigation of the CaO–Al_2O_3–SiO_2 system at high P and T through polymer chemistry and convex-hull techniques. Chemical Geology, 346, 81–92.

Papike, J.J., Burger, P.V., Bell, A.S., Le, L., Shearer, C.K., Sutton, S.R., Jones, J., and Newville, M. (2013) Developing vanadium valence state oxybarometers (spinel-melt, olivine-melt, spinel-olivine) and V/(Cr+Al) partitioning (spinel-melt) for martian olivine-phyric basalts. American Mineralogist, 98, 2193–2196.

Peng, K.W., Zhang, P., Xie, J.G., and Ma, H.L. (2012) Study on properties of Al_2O_3-CaO-SiO_2-CaF_2 slag system. Advanced Materials Research, 396-398, 786–790.

Rakotondrazafy, M.A., Moine, B., and Cuney, M. (1996) Mode of formation of hibonite ($CaAl_{12}O_{19}$) within the U-Th skarns from the granulites of S-E Madagascar. Contributions to Mineralogy and Petrology, 123(2), 190–201.

Righter, K., Sutton, S.R., Newville, M., Le, L., Schwandt, C.S., Uchida, H., Lavina, B., and Downs, R.T. (2006) An experimental study of the oxidation state of vanadium in spinel and basaltic melt with implications for the origin of planetary basalt. American Mineralogist, 91, 1643–1656.

Segev, A., and Rybakov, M. (2011) History of faulting and magmatism in the Galilee (Israel) and across the Levant continental margin inferred from potential field data. Journal of Geodynamics, 51(4), 264–284.

Simon, S.B., Sutton, S.R., and Grossman, L. (2007) Valence of titanium and vanadium in pyroxene in refractory inclusion interiors and rims. Geochimica et Cosmochimica Acta, 71(12), 3098–3118.

Tuff, J., Wood, B.J., and Wade, J. (2011) The effect of Si on metal-silicate partitioning of siderophile elements and implications for the conditions of core formation. Geochimica et Cosmochimica Acta, 75, 673–690.

Xiong, Q., Griffin, W.L., Huang, J.X., Gain, S.E.M., Toledo, V., Pearson, N.J., and O'Reilly, S.Y. (2017) Super-reduced mineral assemblages in "ophiolitic" chromitites and peridotites: the view from Mount Carmel. European Journal of Mineralogy, 29(4), 557–570.

Yoneda, S., and Grossman, L. (1995) Condensation of CaO-MgO-Al_2O_3-SiO_2 liquids from cosmic gases. Geochimica et Cosmochimica Acta, 59(16), 3413–3444.

Endnote:

[1]Deposit item AM-19-26733, Supplemental Material. Deposit items are free to all readers and found on the MSA web site, via the specific issue's Table of Contents (go to http://www.minsocam.org/MSA/AmMin/TOC/2019/Feb2019_data/Feb2019_data.html).